

e^+ and \bar{p} production in pp collisions and the cosmic-ray e^+/\bar{p} ratioKfir Blum,^{1,2} Ryosuke Sato,¹ and Masahiro Takimoto^{1,3}¹*Department of Particle Physics and Astrophysics, Weizmann Institute of Science, Rehovot 7610001, Israel*²*CERN, Theoretical Physics Department, Geneva CH-1211, Switzerland*³*Institute of Particle and Nuclear Studies, High Energy Accelerator Research Organization (KEK), Tsukuba 305-0801, Japan*

(Received 15 May 2018; published 27 September 2018)

The secondary astrophysical production of e^+ and \bar{p} cosmic rays is considered. Inclusive π^- , K^- , and \bar{p} -production cross sections in pp collisions at large \sqrt{s} are parametrized using recent experimental data at LHC energies. The astrophysical production-rate ratio $Q_{e^+}/Q_{\bar{p}}$ is calculated for an input cosmic ray proton flux consistent with local measurements. At $10 < E < 100$ GeV, the cosmic ray flux ratio $J_{e^+}/J_{\bar{p}}$ measured by AMS02 falls below the production-rate ratio by about 50%, while at high energy $E > 100$ GeV, the measured flux ratio coincides with the production-rate ratio of the secondary source.

DOI: [10.1103/PhysRevD.98.063022](https://doi.org/10.1103/PhysRevD.98.063022)**I. INTRODUCTION**

Cosmic ray (CR) antimatter is a potential probe of exotic high-energy astrophysical phenomena and a unique diagnostic of CR propagation. Over the last decade, precise measurements of the flux of CR e^+ and \bar{p} extending to ever higher energies were reported by the PAMELA and AMS02 experiments [1–3]. The interpretation of these measurements motivates refined theoretical consideration of astrophysical e^+ and \bar{p} , produced as secondaries in the collision of primary CRs, notably protons, with interstellar matter (ISM), notably hydrogen. Our goal in the current paper is to improve on previous calculations of the inclusive production cross section of secondaries in pp collisions using recent accelerator data.

The main effect we wish to capture is the violation of radial scaling at $\sqrt{s} > 50$ GeV. As shown in Refs. [4–6], this effect leads to about a factor-of-2 increase in the astrophysical \bar{p} source at \bar{p} energy above a few TeV. Here we evaluate the analogous effect in the CR e^+ source by analyzing meson production at LHC energies. Earlier e^+ calculations either were based on data taken at \sqrt{s} too low to see the effect [7–9] or relied on Monte Carlo tools without direct verification in the kinematical regime relevant for astrophysics [10].

We aim to achieve $\sim 10\%$ accuracy for the astrophysical e^+ source at e^+ energy ranging from a few GeV up to multi-TeV; this accuracy goal is to be compared with the main

radial scaling violation effect that is, again, about a factor of 2 at $E \sim 10$ TeV. As a check against earlier work, we also calculate the \bar{p} source to similar accuracy. Rather than attempting to cover in detail the whole kinematics of secondary production, we aim specifically at integrated moments of the cross section that are directly related to cosmic ray yields, a simplification that allows us to use relatively simple and easy-to-implement fitting formulas. Moreover, we focus our attention on high-energy secondary CR with relativistic observer frame energies. This further simplifies the analysis.

In Sec. II, we analyze the cross sections at large \sqrt{s} , using results from the NA49, PHENIX, BRAHMS, ALICE, and CMS experiments. In Sec. III, we use these results to calculate the production-rate ratio $Q_{e^+}/Q_{\bar{p}}$ for secondary e^+ and \bar{p} produced by a spectrum of high-energy protons scattering on a proton target. We show that $Q_{e^+}/Q_{\bar{p}}$ is insensitive with respect to uncertainties in the primary proton spectrum. At $10 < E < 100$ GeV, the e^+/\bar{p} flux ratio measured by AMS02 falls below the production-rate ratio by about 50%, while at high energy $E > 100$ GeV, the measured flux ratio coincides with the production-rate ratio of the secondary source. In Appendix A, we discuss the contribution to secondary e^+ from K_L^0 decay, which was missing in previous calculations. In Appendix B, we analyze the hyperon contribution to inclusive \bar{p} production. In Appendix C, we reproduce the secondary cosmic ray \bar{p} flux predicted by using mean traversed target column density as deduced from cosmic ray nuclei data.

II. DATA ANALYSIS

Our baseline fitting formulas for inclusive hadron production in pp collisions are taken from Ref. [11]

Published by the American Physical Society under the terms of the Creative Commons Attribution 4.0 International license. Further distribution of this work must maintain attribution to the author(s) and the published article's title, journal citation, and DOI.

(Tan and Ng), which was based on $\sqrt{s} \leq 53$ GeV data and to which we provide corrections using the following new information:

- (i) Tan and Ng's formulas rely on radial scaling [12–14],

$$E \frac{d^3\sigma}{dp^3}(x_R, p_t, \sqrt{s}) \rightarrow_{\sqrt{s} \rightarrow \infty} E \frac{d^3\sigma}{dp^3}(x_R, p_t), \quad (1)$$

where $x_R = E^*/E_{\max}^*$, E^* is the final-state hadron energy in the center-of-mass frame, and E_{\max}^* is the maximum attainable E^* . Recent accelerator data [15–20] show violation of radial scaling in pp collisions at $\sqrt{s} \gtrsim 50$ GeV. The $pp \rightarrow \bar{p}$ cross section increases at high energy [4–6] as compared to Ref. [11] and other early parametrizations. We will assess the analogous effect in meson production and the resulting e^+ yield.

- (ii) In addition to the high-energy end, unprecedented detail in measurements of the production cross sections for π^+ , K^\pm , and \bar{p} [21–23] at $\sqrt{s} = 17.2$ GeV was reported by the NA49 experiment. This value of \sqrt{s} is particularly relevant for the $E \sim 10$ – 100 GeV final-state \bar{p} and e^+ [24]. We incorporate these data in our formulas for hadronic cross sections.

A. p_t -weighted cross sections and the important kinematical region for relativistic secondary CRs

Faced with an extensive data set [15–23], it is instructive to bracket the final-state phase space that is most relevant for secondary CR production. For this purpose it is useful to consider a few approximations. To avoid confusion, we emphasize that these approximations [given below in Eq. (4), and in the power-law approximation for the CR proton flux that we use in the second line of Eq. (5)] are only used in the current section to highlight the important part of the physics. We do not employ these approximations in our actual cross-section parametrization. In particular, our results are applicable for arbitrary primary proton spectra and are not limited to the power-law form.

In the fixed-target setup of high-energy CR scattering on ambient ISM, the key quantity is the conversion cross section from an incoming CR proton with ISM frame energy E_p to an outgoing secondary particle with ISM frame energy E :

$$\frac{d\sigma(E_p, E)}{dE} = 2\pi \int_0^\pi d\theta p_t \left(E \frac{d^3\sigma}{dp^3} \right) (x_R, p_t, \sqrt{s}), \quad (2)$$

where θ denotes the angle between the incoming proton and the outgoing secondary particle in the ISM frame. The Lorentz-invariant differential cross section $E \frac{d^3\sigma}{dp^3}$ decreases sharply with increasing p_t , with the p_t -weighted cross section $p_t \left(E \frac{d^3\sigma}{dp^3} \right)$ peaking around an average of

$\langle p_t \rangle \sim 0.2$ – 0.4 GeV. For $E \gg \langle p_t \rangle$, m , where m is the mass of the final-state hadron of interest, we can simplify the integral as

$$\int_0^\pi d\theta p_t \left(E \frac{d^3\sigma}{dp^3} \right) (x_R, p_t, \sqrt{s}) \simeq \frac{1}{p} \int_0^\infty dp_t p_t \left(E \frac{d^3\sigma}{dp^3} \right) (x_R|_{p_t=0}, p_t, \sqrt{s}), \quad (3)$$

where $x_R|_{p_t=0}$ is computed at $p_t = 0$ and only depends on E and E_p . This exercise shows that, in the high-energy regime, the p_t -weighted mean cross section with fixed x_R is the most important quantity for secondary CR production, allowing one to average over the detailed p_t dependence reported by the experiments.

Next, we consider the relevant range of x_R . Consider as a representative example the cross-section parametrization [5]

$$E \frac{d^3\sigma}{dp^3}(x_R, p_t) = f_0 e^{-\frac{p_t}{\langle p_t \rangle}} (1 - x_R)^n. \quad (4)$$

Typical parameters are $\langle p_t \rangle \simeq 0.2$ – 0.4 GeV and $n \simeq 5$ – 7 . In the limit where $m/E \ll 1$, $p_t^2/E^2 \ll 2m_p/E_p$, we have the relation $E \simeq E_p x_R$, where E and E_p denote the energy of the secondary particle and that of the incoming proton in the ISM frame and x_R is defined in the c.m. frame. Then, the astrophysical source term $Q(E)$ can be written as

$$Q(E) \propto \int_E^\infty dE_p J_p(E_p) \frac{d\sigma(E_p, E)}{dE} \simeq 2\pi f_0 \langle p_t \rangle^2 J_p(E) \int_0^1 dx_R x_R^{\gamma-2} (1 - x_R)^n, \quad (5)$$

where J_p denotes the CR proton flux and we assume $J_p \propto E_p^{-\gamma}$. With $n \simeq 5$ – 7 and $\gamma \simeq 2.7$, the x_R integrand selects the range ~ 0.1 – 0.4 .

To summarize, we are most interested in the cross section for secondary product (observer-frame) energy in the range $E \gtrsim 10$ GeV. In this range, the relevant information is contained in the p_t -weighted mean invariant cross section at fixed x_R , where furthermore the relevant range of x_R is ~ 0.1 – 0.4 .

B. Hadron-production cross section

In this section, we discuss the hadronic cross section in the light of recent collider experiments. We take the cross-section fits by Tan and Ng as a baseline, and then derive corrections to these formulas.

A comment is in order regarding the intermediate hyperon contribution to \bar{p} . In pp collisions, \bar{p} 's are generated promptly or by the decay of (relatively) long-lived hyperons, notably $\bar{\Lambda}$ and $\bar{\Sigma}^\pm$. The Tan-Ng \bar{p} fit

includes the hyperon contributions. On the other hand, recent experiments such as NA49 report the prompt antiproton cross section in which the contribution of intermediate hyperon states is removed. Thus, when comparing experimental \bar{p} cross-section data and fits, we need to specify whether the hyperon contribution is subtracted or not. For the purpose of astrophysical calculations, of course, our eventual concern is the total \bar{p} cross section, including the hyperon contributions. In this section, however, we find it convenient to concentrate first on the prompt \bar{p} -production cross section, deferring an analysis of the hyperon contribution to Appendix B.

1. NA49 experiment

The NA49 experiment reported measurements in a wide kinematic regime. Figure 1 shows measurements of the p_t -weighted and integrated cross section, presented as a ratio between NA49 data and the Tan-Ng formulas in given x_F bins.¹ The quantity we present in the plot is the ratio of the p_t -weighted and integrated cross section at fixed x_F —that is, we numerically perform the integral in the second line of Eq. (3), once using the Tan-Ng cross-section fit and then again directly from the experimental data. We use data from Refs. [21,22,23] for π^+ , K^\pm , and \bar{p} , respectively. For each point in Fig. 1, the uncertainty is dominantly systematic, about 4.8% for π^+ and 6.5% for \bar{p} (see Table 3 in Ref. [21] and Table 2 in Ref. [23]).

As we discussed, the most relevant kinematical region for determining the CR secondary source is $x_F = 0.1$ – 0.4 . In this region, Fig. 1 shows that apart from an overall factor, the fitting functions of Tan and Ng are consistent with the NA49 results for all final states with the possible exception of K^- (the latter being quantitatively irrelevant for the secondary e^+ calculation). Motivated by this result, we introduce a scaling factor $\xi_H(\sqrt{s})$ for each hadron $H = \pi^+$, K^\pm , \bar{p} , and parametrize the cross section as

$$E \frac{d^3\sigma_H}{dp^3} = E \frac{d^3\sigma_H}{dp^3} \Big|_{\text{Tan-Ng}} \times \xi_H(\sqrt{s}). \quad (6)$$

Based on the NA49 analysis in Fig. 1, we take $\xi_{\pi^+} = 0.9$ and $\xi_{\bar{p}} = 0.8$ at $\sqrt{s} = 17.2$ GeV. Again from Fig. 1, we assign an uncertainty of 10% to these values of ξ_{π^+} , \bar{p} . This uncertainty estimate is slightly larger than the nominal measurement uncertainty quoted by NA49, but it is motivated by the detailed structure in Fig. 1 that deviates from a constant normalization factor at the 10% level. Finally, to avoid excess detail, we set $\xi_{K^\pm} = \xi_{\pi^+}$, as further corrections due to the kaon contribution to e^+ production are insignificant.

¹NA49 data are provided in terms of the Feynman parameter $x_F = 2p_L^*/\sqrt{s}$ (where p_L^* is the hadron longitudinal momentum in the c.m. frame) instead of x_R , so we consider the p_t -weighted cross section at fixed x_F .

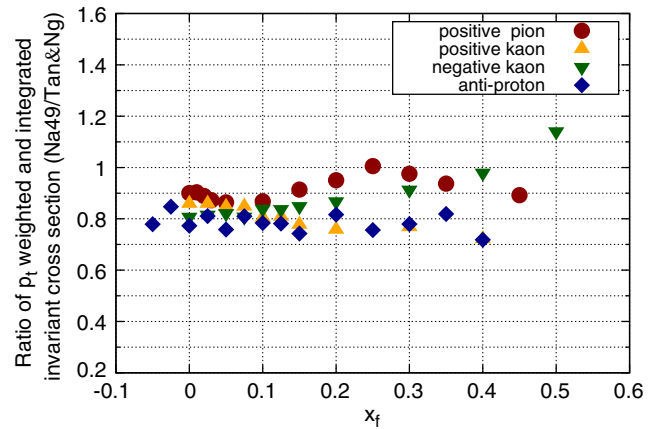


FIG. 1. p_t -weighted and integrated cross sections for π^+ , K^\pm and \bar{p} , presented as the ratio between NA49 data [21–23] and Tan-Ng [11] inclusive cross-section formulas, in given x_F bins. Note that the Tan-Ng formulas include contributions from unstable intermediate states, such as the hyperon contribution $\bar{\Lambda} \rightarrow \bar{p}\pi^+ \rightarrow \bar{p}$ production, that is subtracted in the NA49 \bar{p} data. We explain how to correct for this effect in the text.

In Ref. [5], a change in p_t dependence is also taken into account. For the secondary cosmic ray flux, the p_t -weighted cross section as given in Eq. (2) is important. Here we take a simple modification given in Eq. (6).

Note that the prompt \bar{p} cross section from NA49 is off by $\sim 20\%$ from the inclusive Tan-Ng fit: this is not a discrepancy, but is mainly due to the hyperon contribution present in the Tan-Ng fit while being subtracted from NA49 data. Accounting for this correction, we find, in fact, that the inclusive Tan-Ng fit is in good agreement with that deduced from NA49 data.

2. High-energy experiments

Next, we analyze the high-energy data to determine the behavior of ξ_H at large \sqrt{s} . The scaling factors ξ_H are calibrated to reproduce the p_t -weighted cross section of Eq. (3) evaluated on the high-energy experimental data. Our results are summarized by the correction functions given in Eqs. (7)–(9). We now explain the analysis.

Figure 2 shows the \sqrt{s} dependence of ratios of p_t -weighted cross sections for π^+ , K^\pm (top panel), and \bar{p} (bottom panel) between high-energy data and the Tan-Ng formulas [11]. Solid lines indicate the correction functions of Eqs. (7)–(9). We use data from PHENIX [19] at $\sqrt{s} = 62.4, 200$ GeV; from CMS [18] at $\sqrt{s} = 900, 2760, 7000$ GeV; from ALICE [15,17] at $\sqrt{s} = 900, 7000$ GeV; and from the BRAHMS [20] analysis at $\sqrt{s} = 200$ GeV.

We calculate the p_t -weighted cross section using the p_t range provided by the experiments. Since CMS and ALICE give a production yield, we use a fitting function of the inelastic total scattering cross section, taken from Ref. [5], to obtain the cross section. In addition, to obtain an inelastic yield for CMS, we multiply an empirical factor

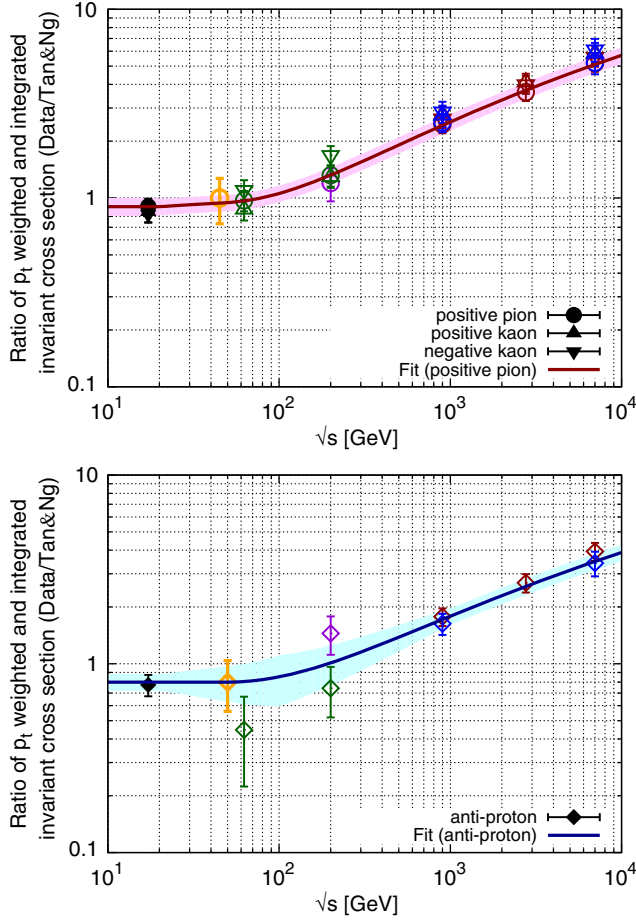


FIG. 2. \sqrt{s} dependence of ratios of p_t -weighted cross sections for π^+ , K^\pm (top panel), and \bar{p} (bottom panel) between high-energy experiments and Tan and Ng's formulas [11]. Solid lines indicate the correction functions ξ_H , and the shaded band indicates an estimated 1σ uncertainty range. Black, green, blue, red, and purple points correspond to NA49 [21–23], PHENIX [19], ALICE [15,17], CMS [18], and BRAHMS [20] data, respectively. The orange points represent a summary of the data sets used in the Tan-Ng analysis [11].

0.78 (see Ref. [18]). For ALICE data, we use dN/dy estimated in Refs. [15,17]. Statistical and systematic errors are roughly 10% for all experiments apart from the PHENIX \bar{p} data and the BRAHMS forward rapidity data, to which we refer in more detail below.

The orange points in Fig. 2 (centered at $\sqrt{s} = 45$ GeV) summarize the collection of early experimental data used by the Tan-Ng original analysis [11]. These early measurements cover a wide range of phase space and energy, corresponding to $\sqrt{s} \simeq 10$ –60 GeV. Detailed consideration shows that the Tan-Ng fits are consistent with these data to within $\sim \pm 30\%$, comparable to the variation between the results of individual analyses in this data set, and we assign this uncertainty to the orange points. A summary of the experimental data entering the Tan-Ng fit for \bar{p} is shown in Fig. 3. The scatter is similar for the meson analysis.

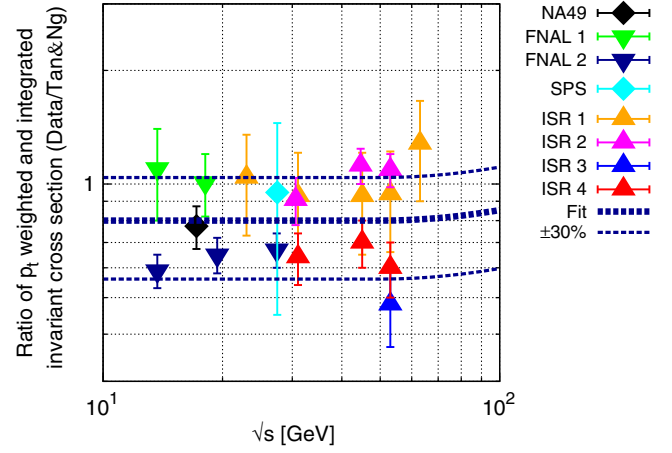


FIG. 3. Evaluation of the experimental data used in the Tan-Ng analysis [11] for fitting the \bar{p} -production cross section. Note that the plot compares prompt \bar{p} data, extracted from each experimental reference using the procedure of Appendix B, to the inclusive (prompt + nonprompt) Tan-Ng fit. References: SPS [25], ISR 1 [26], ISR 2 [27], ISR 3 [28], ISR 4 [29], FNAL 1 [30], FNAL 2 [31].

We find that the correction functions

$$\xi_{\pi^+} = 0.9 + 0.05 \log\left(\frac{\sqrt{s}}{20 \text{ GeV}}\right) \theta(\sqrt{s} - 20 \text{ GeV}) + 0.16 \log^2\left(\frac{\sqrt{s}}{50 \text{ GeV}}\right) \theta(\sqrt{s} - 50 \text{ GeV}), \quad (7)$$

$$\xi_{\bar{p}} = 0.8 + 0.11 \log^2\left(\frac{\sqrt{s}}{50 \text{ GeV}}\right) \theta(\sqrt{s} - 50 \text{ GeV}), \quad (8)$$

$$\xi_{K^\pm} = \xi_{\pi^+} \quad (9)$$

reproduce the experimentally determined p_t -weighted and integrated cross sections in the range $\sqrt{s} \leq 7$ TeV. Our estimated 1σ uncertainty range for the ξ_H functions, determined from the uncertainties in the analyzed data, is shown by the shaded bands in Fig. 2.

Several comments are in order. First, the PHENIX \bar{p} data [19] in Fig. 2 exhibit larger uncertainty compared to most of the other measurements, and the central values are indeed correspondingly off by $\sim 50\%$, 30% for $\sqrt{s} = 62.4$ and 200 GeV from the fit. To estimate the p_t -weighted \bar{p} cross section from Ref. [19], we start with the data without feed-down correction, as the feed-down-corrected cross section is found to be lower by a factor of a few in low- p_t bins, which appears broadly inconsistent with the remaining data set. To estimate the feed-down-corrected result, we subtract 30% off the inclusive result, as suggested by our analysis in Appendix B. The \bar{p} systematic uncertainties quoted in Ref. [19] are sizable, notably in the lower- p_t region, due to the feed-down correction and take maximally $\sim 50\%$, 30% for $\sqrt{s} = 62.4$ and 200 GeV. In Fig. 2, we

assign these conservative uncertainty estimates of 50% and 30% to these data. In addition to the feed-down uncertainty, the p_t range covered by the \bar{p} cross-section data in Ref. [19] is limited, starting from $p_t = 0.6$ GeV. This means that the p_t -weighted cross-section estimate derived from these data is based on a kinematically subdominant region for astrophysical purposes.

Second, the BRAHMS analysis [20] is special, in that it contains forward rapidity data at $y = 2.95$ and $y = 3.3$. This data set was given for a range of p_t values at fixed rapidity. To extract our key quantity—a p_t -weighted cross section at fixed x_R (or x_F)—we use a limited subset of the data with $p_t < 1$ GeV. For this range of p_t , the range of x_F for π^+ (\bar{p}) in the $y = 2.95$ data set is limited to $0.03 < x_F < 0.1$ ($0.1 < x_F < 0.13$). Comparing with NA49 data [21,23], we expect that the variation of the Lorentz invariant cross section across this limited range of x_F is smaller than 30% for both π^+ and \bar{p} . We check that varying the maximal p_t in the analysis within $0.8 \text{ GeV} < p_t < 1.2 \text{ GeV}$ affects our results by less than 20%. The final uncertainty we assign to our analysis of BRAHMS data, 20% for π^+ and 23% for \bar{p} , is adopted from Ref. [20]. We do not use the $y = 3.3$ data set, which contains a significantly smaller usable range of p_t at small x_F .

Third, we comment on the K_S contribution to the π cross section. In the analysis of Fig. 2, we assume that the π cross sections reported by the experiments are prompt and do not include π 's from K_S decay. The NA49 and CMS experiments explicitly state that π 's from K_S decay are discriminated in their analyses. On the other hand, the treatment in the PHENIX and ALICE experiment is unclear. This makes a 5% ambiguity of the points from the PHENIX and ALICE experiments in Fig. 2. In practice, this ambiguity is not quantitatively important for the determination of the fitting formula.

Fourth, we comment on the x_R dependence in the high- \sqrt{s} regime. The high-energy experimental data from Refs. [15,17–19] is only specified at midrapidity ($x_R \simeq 0$). This means that our fit could fail to reproduce the x_R dependence in the high- \sqrt{s} regime. Fixing this caveat would require cross-section data at nonzero x_R (forward region) in the high- \sqrt{s} regime. The overall consistency of our fit with the BRAHMS data [20] suggests that this effect is not too significant.

Finally, it is important to comment in general that in focusing our analysis on the p_t -weighted and integrated cross section, using the simple \sqrt{s} -dependent, but p_t -independent correction factors ξ_H that come as multiplicative correction to the Tan-Ng parametrization [11], we are likely to miss detailed kinematical features of the cross section: our cross-section formulas will not reproduce the detailed p_t spectra of secondary hadrons. However, the use we designate for our fitting functions is for high-energy [$E > 10$ GeV; see the discussion around Eq. (3)] secondary CR production, and here we expect our simple fit in

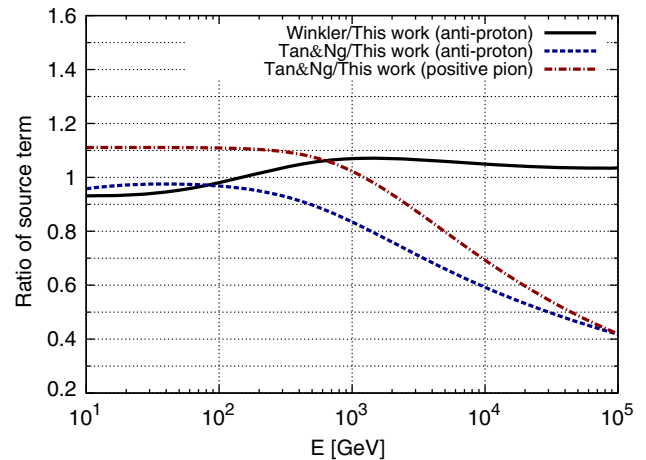


FIG. 4. Final-state (undecayed, in the case of pions, and decayed, in the case of \bar{p}) energy dependence of the ratios of source terms assuming $J_p \propto E_p^{-3}$. The black line shows the \bar{p} source-term ratio between that obtained using the fit of Ref. [5] (denoted “Winkler”) and ours. The blue dotted (red dashed) line shows the \bar{p} (π^+) source-term ratio between Tan and Ng’s [11] and ours.

Eqs. (7)–(9) to produce the correct secondary production rate within the uncertainties shown in Fig. 2.

C. Astrophysical source terms, and comparison to previous work

The astrophysical source terms for secondary \bar{p} and e^+ produced in pp collisions, specified in terms of production-rate spectrum per single proton target, are given by²

$$Q_{\bar{p}}(E_{\bar{p}}) = 2 \int_{E_{\bar{p}}}^{\infty} dE_p 4\pi J_p(E_p) \frac{d\sigma_{pp \rightarrow \bar{p}}(E_p; E_{\bar{p}})}{dE_{\bar{p}}}, \quad (10)$$

$$Q_{e^+}(E_{e^+}) = \int_{E_{e^+}}^{\infty} dE_p 4\pi J_p(E_p) \frac{d\sigma_{pp \rightarrow e^+}(E_p; E_{e^+})}{dE_{e^+}}. \quad (11)$$

In Fig. 4, we show the secondary source terms for \bar{p} and π^+ , assuming pp production from a power-law primary proton flux $J_p \propto E_p^{-3}$, comparing our results to the fitting formulas of Ref. [5] and Tan and Ng. Here, for simplicity, we take a simple power-law proton flux. This is sufficient for the purpose of comparing our results with previous work; below we will show results using proton and nuclei flux directly from data. Furthermore, to highlight the difference with previous work, we use here the central value for our cross-section fits. For \bar{p} production, we include the contributions from both hyperon decay and decay in the flight of \bar{n} , using the procedure defined in Appendix B. The black line shows the \bar{p} source-term ratio

²Note that (i) the factor 2 in $Q_{\bar{p}}$ comes from decay in the flight of \bar{n} , and (ii) the normalization in our definition for $Q_{e^+, \bar{p}}$ here is somewhat different than in, e.g., Refs. [24,32,33]. This is for ease of presentation and is of no consequence for the source ratio.

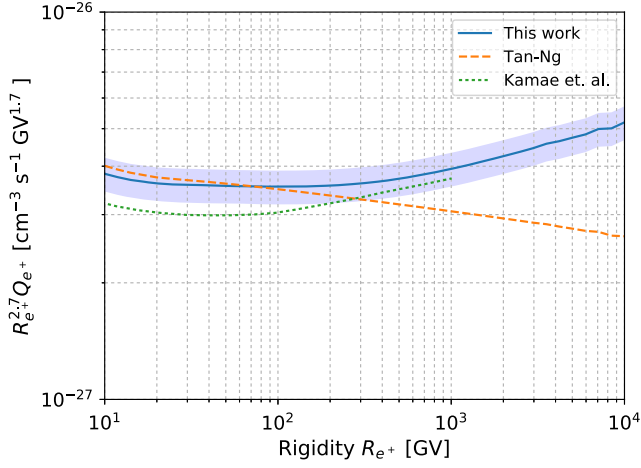


FIG. 5. Comparison of the e^+ source term computed with different cross-section parametrizations. Green dotted line: calculation from Ref. [8] using the cross section from Ref. [10]. Orange dashed line: calculation using Tan and Ng’s pion and kaon production fit. Blue solid line: our result in this work. The shaded band shows the calculation uncertainty, derived by folding the uncertainties in our cross-section parametrization into the source-term expressions of Eqs. (10) and (11). All calculations include only pp collisions and are done—for concreteness—using the primary proton spectrum from Ref. [35].

between that obtained using the fit of Ref. [5] (denoted “Winkler”) and ours. We find agreement to the 10% level. The blue dotted (red dashed) line shows the \bar{p} (π^+) source-term ratio between Tan and Ng’s [11] and ours. The deviation from radial scaling, assumed in Tan and Ng, is clear at high energy.

Next, we consider the decayed final-state e^+ source term, obtained after taking into account the decay in the flight of pions and kaons. In Fig. 5, we show the e^+ source term per target proton, derived in Ref. [8] using the e^+ -inclusive cross section computed with the PYTHIA [34] fit of Ref. [10] (dotted green) for the primary proton spectrum of Ref. [35]. In addition, we show the source terms obtained using the Tan-Ng parametrization (orange dashed) and using our fit result derived in this paper (solid blue). The shaded band shows the calculation uncertainty, derived by folding the uncertainties in our cross-section parametrization into the source-term expressions of Eqs. (10) and (11). At high e^+ rigidity, $\mathcal{R} \gtrsim 300$ GV, our result is in very good agreement with the result of Ref. [8] using the formulas from Ref. [10]. This suggests that the PYTHIA-based calculation accounts well for the radial scaling violation effect. At lower e^+ energy, our result is in better agreement with the data-driven fit of Tan and Ng.

III. e^+/\bar{p} SOURCE-TERM RATIO VS OBSERVED e^+/\bar{p} FLUX RATIO

Reference [32] pointed out that the production-rate ratio $Q_{e^+}/Q_{\bar{p}}$ provides a model-independent upper

bound to the flux ratio of high-energy secondary CR e^+ and \bar{p} :

$$\frac{J_{e^+}(\mathcal{R})}{J_{\bar{p}}(\mathcal{R})} < \frac{Q_{e^+}(\mathcal{R})}{Q_{\bar{p}}(\mathcal{R})}. \quad (12)$$

This upper bound only depends on the inclusive production cross sections and the shape of proton cosmic ray flux J_p .

We are now in position to extend the calculation of $Q_{e^+}(\mathcal{R})/Q_{\bar{p}}(\mathcal{R})$ to high energy, and compare with the latest CR data. In Fig. 6, we show the upper bound predicted for different assumptions on the primary proton flux in the spallation region. For this calculation, in addition to p - p collision, we consider p -He, He- p , and He-He collisions. The e^+/\bar{p} flux ratio measured by AMS-02 is consistent with the upper bound and saturates it at high energy (for proton flux coinciding with the locally measured proton flux, for which we use Refs. [36,37]). Model examples for secondary e^+ and \bar{p} , including scenarios where the proton spectrum at the secondary production sites is different from the locally measured spectrum, include Refs. [32,38–51].

Recent calculations of the high-energy secondary CR \bar{p} flux [5,6,24], using an up-to-date \bar{p} production cross section consistent with our results here and calibrated to agree with AMS-02 B/C data, are consistent with the CR \bar{p} flux measured by AMS-02. These results are reproduced in Appendix C. The significance, in connection with Fig. 6, is that the observed flux of CR e^+ at $\mathcal{R} > 100$ GV coincides with the expected flux of secondary e^+ , that would be expected if radiative energy loss became unimportant in the

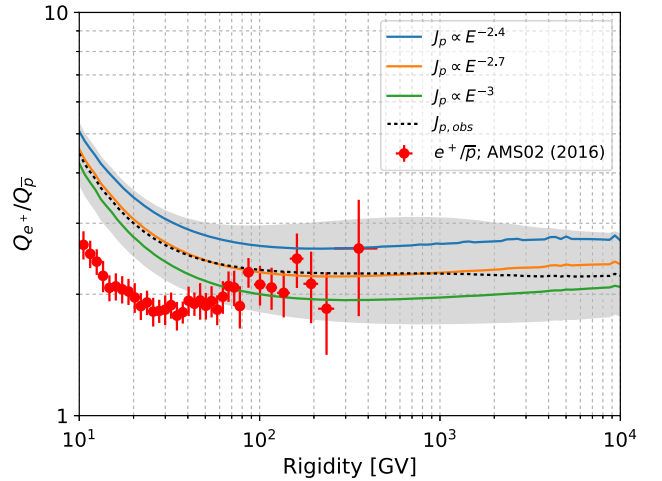


FIG. 6. The ratio of $Q_{e^+}/Q_{\bar{p}}$. The dashed line is calculated by using the observed (non-power-law) proton flux, for which we use Refs. [36,37]. The width of the shaded region shows the calculation uncertainty, derived by folding the uncertainties in our cross-section parametrization into the source-term expressions of Eqs. (10) and (11). The blue, orange, and green solid lines are calculated by assuming $J_p \propto E^{-2.4}$, $E^{-2.7}$, and E^{-3} , respectively. The observational data e^+/\bar{p} are taken from Ref. [3].

propagation at these energies. Achieving such a low level of energy loss would require that the characteristic secondary CR propagation time drop below a few Myr at $\mathcal{R} > 100$ GV.

We note that steady-state disc + halo diffusion models, widely used in the literature (see Ref. [52] for a review), assume a CR propagation time t_{esc} that scales with \mathcal{R} similarly to the CR grammage X_{esc} .³ Stable nuclei data (notably B/C) imply $X_{\text{esc}} \sim \mathcal{R}^{-0.4}$ or so [33], while radioactive nuclei elemental ratios (Be/B, Al/Mg, Cl/Ar) imply a propagation time of the order of tens of Myr at $\mathcal{R} \sim 10$ GV [53,54]. A rapid drop in t_{esc} , from ~ 10 Myr at $\mathcal{R} = 10$ GV to ~ 1 Myr at $\mathcal{R} = 100$ GV, would contradict the prediction of these diffusion models [32].

A comparison of the source ratio $Q_{e^+}/Q_{\bar{p}}$ to the observed e^+/\bar{p} flux ratio was also presented in Ref. [55], which found results for $Q_{e^+}/Q_{\bar{p}}$ smaller than our value by $\sim 30\%$ in the energy range 10–1000 GeV. This led Ref. [55] to argue that e^+ energy losses may be negligible at all energies (rather than only at $E \gtrsim 100$ GeV, as suggested by our Fig. 6). We have not been able to reproduce the origin of this discrepancy.

IV. CONCLUSIONS

We presented an analysis of inclusive \bar{p} , π , and K production in pp collisions. Our main goal was to implement recent experimental data for meson production—in particular, the effect of radial scaling violation manifest at LHC energies and recent detailed kinematical data from the NA49 experiment at intermediate energy, in semianalytic fits used for the calculation of the astrophysical secondary production of e^+ . We provide fitting formulas that, combined with earlier results from Tan and Ng [11], allow us to compute the astrophysical production of e^+ and \bar{p} up to the multi-TeV range with an estimated uncertainty of $\sim 20\%$.

The e^+/\bar{p} flux ratio reported by AMS-02 is found to coincide with the secondary source production-rate ratio $Q_{e^+}/Q_{\bar{p}}$ at high-energy $E > 100$ GeV.

ACKNOWLEDGMENTS

This research is supported by Grant No. 1937/12 from the I-CORE program of the Planning and Budgeting Committee and the Israel Science Foundation, and by Grant No. 1507/16 from the Israel Science Foundation. The work of M. T. is supported by the JSPS Research Fellowship for Young Scientists. K. B. is incumbent of the

³This follows from the assumption of \mathcal{R} -independent boundary conditions in these models. For the usual disc + halo diffusion model with a CR free-escape vertical boundary at L , $X_{\text{esc}} \approx X_{\text{disc}} cL/D(\mathcal{R})$ and the propagation time $t_{\text{esc}} \approx L^2/2D(\mathcal{R}) \propto X_{\text{esc}}$, where $D(\mathcal{R})$ is the diffusion coefficient and X_{esc} is the grammage of the thin gas disc.

Dewey David Stone and Harry Levine career development chair.

APPENDIX A: NEUTRAL KAON CONTRIBUTIONS

In this appendix, we calculate the final-state e^+ contribution coming from the decay of K_L^0 mesons. This contribution has been neglected in the literature, although the corresponding cross section is comparable to that for charged kaons, which was previously taken into account. K_L^0 mesons are long lived ($c\tau_{K_L^0} \simeq 15$ m) in the collider setup, so that π^+ 's from K_L^0 decay are not included in the fitting formula of the inclusive π^+ cross section. In addition, the K_L^0 semileptonic decay contributes directly to e^+ and $\mu^+(\rightarrow e^+)$ production.

We consider the following decay channels [56]:

$$\text{Br}(K_L^0 \rightarrow \pi^\pm e^\mp \nu_e) = 40.55\%, \quad (\text{A1})$$

$$\text{Br}(K_L^0 \rightarrow \pi^\pm \mu^\mp \nu_e) = 27.04\%, \quad (\text{A2})$$

$$\text{Br}(K_L^0 \rightarrow \pi^+ \pi^- \pi^0) = 12.54\%. \quad (\text{A3})$$

We approximate and simplify the kinematics of K_L^0 three-body decays, assigning each of the decay products an energy of $m_K/3$ in the K_L^0 rest frame and ignoring muon polarization. (These approximations are valid to better than 20%.) We approximate the K_L^0 -production cross section to match that of K^+ . The e^+ spectrum from boosted μ^+ is given in Ref. [57], and the e^+ spectrum from boosted π^+ is given in Ref. [58].

The kaon contribution to astrophysical secondary e^+ production is highlighted in Fig. 7. The K_L^0 contribution amounts roughly to 5% of the total e^+ source. π^0 also can

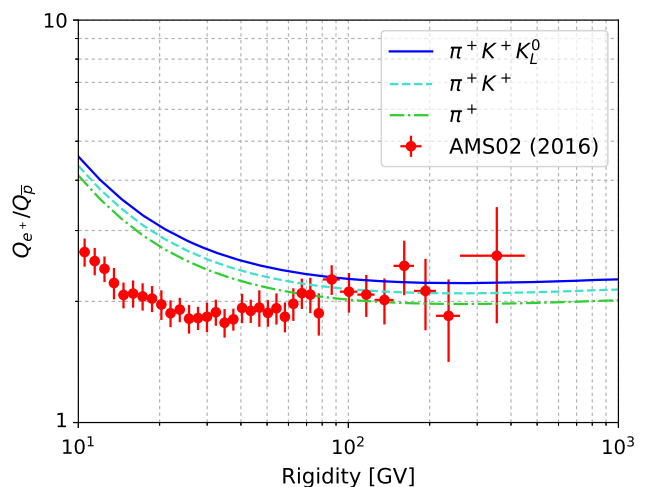


FIG. 7. Same as in Fig. 6, but highlighting the kaon contribution to the source term of secondary e^+ . The proton spectrum is assumed to follow $J_p \propto E^{-2.7}$.

contribute to the e^+ flux; however, the dominant channel is $e^+e^-\gamma$, and its branching fraction is 1.2% [56]. We can expect that the π^0 contribution to the e^+ source term is $\sim 1\%$ of π^+ , and we neglect this contribution.

APPENDIX B: ANTIPROTON CROSS SECTION INCLUDING ANTIHYPERON CONTRIBUTIONS

In this appendix, we analyze the hyperon contribution to the inclusive \bar{p} -production cross section. We denote the Lorentz-invariant differential cross section as f :

$$f_{\#} \equiv E \frac{d^3 \sigma_{\#}}{dp^3}. \quad (\text{B1})$$

The astrophysically relevant inclusive $f_{\bar{p}}^{\text{tot}}$, which includes effects from \bar{n} and hyperon decays, can be decomposed in the following way:

$$f_{\bar{p}}^{\text{tot}} = f_{\bar{p}} + f_{\bar{n}}, \quad (\text{B2})$$

$$f_{\bar{p}} = f_{\bar{p}}^0 + f_{\bar{p}}^{\bar{\Lambda}} + f_{\bar{p}}^{\bar{\Sigma}}, \quad (\text{B3})$$

$$f_{\bar{n}} = f_{\bar{n}}^0 + f_{\bar{n}}^{\bar{\Lambda}} + f_{\bar{n}}^{\bar{\Sigma}}, \quad (\text{B4})$$

where f^0 indicates the prompt contribution and $f^{\bar{\Lambda}, \bar{\Sigma}}$ denote contributions from the hyperon decay. Neglecting isospin violation for prompt nucleons, we assume $f_{\bar{p}}^0 = f_{\bar{n}}^0$. To set a rough scale for the effect we are after here, the analysis in Sec. II shows $f_{\bar{p}}^0 \simeq 0.8 f_{\bar{p}}^{\text{Tan-Ng}}$ at low \sqrt{s} , where $f_{\bar{p}}^{\text{Tan-Ng}}$ includes the hyperon decay contribution. [See Eq. (8) and Fig. 2.]

Before getting to the details, we summarize our final formula for the hyperon-corrected, decayed final-state astrophysical cross section:

$$f_{\bar{p}}^{\text{tot}} = f_{\bar{p}}^{\text{Tan-Ng}} \times [2\xi_{\bar{p}}(\sqrt{s}) + (g_{\bar{\Lambda}} + g_{\bar{\Sigma}^-} + g_{\bar{\Sigma}^+})\kappa(\sqrt{s})]. \quad (\text{B5})$$

The prompt modification function $\xi_{\bar{p}}(\sqrt{s})$ is given in Eq. (8). Analogously, we define the hyperon modification function $\kappa(\sqrt{s})$, which we derive from data in Sec. II of this appendix, with results given by Eqs. (B11) and (B12). The terms g_B , $B = \Lambda, \Sigma^{\pm}$ are additional kinematic correction terms that we parametrize as functions of x_R but not of \sqrt{s} . The derivation of g_B is given in Sec. III of this appendix, with the numerical result summarized in and below Eq. (B18).

1. Antihyperon-production cross section at the NA49 experiment

NA49 [21] results indicate that the kinematical distribution of antihyperons produced in pp collisions is

somewhat different from that of antinucleons.⁴ We introduce x_R -dependent functions $g_B(x_R)$ with $\bar{B} = \bar{\Lambda}, \bar{\Sigma}^{\pm}$, and parametrize the hyperon contributions as

$$f_{\bar{p}}^{\bar{\Lambda}} = f_{\bar{p}}^{\text{Tan-Ng}} \kappa(\sqrt{s}) g_{\bar{\Lambda}}(x_R) \text{Br}(\Lambda \rightarrow pX), \quad (\text{B6})$$

$$f_{\bar{n}}^{\bar{\Lambda}} = f_{\bar{p}}^{\text{Tan-Ng}} \kappa(\sqrt{s}) g_{\bar{\Lambda}}(x_R) \text{Br}(\Lambda \rightarrow nX), \quad (\text{B7})$$

$$f_{\bar{p}}^{\bar{\Sigma}} = f_{\bar{p}}^{\text{Tan-Ng}} \kappa(\sqrt{s}) g_{\bar{\Sigma}^-}(x_R) \text{Br}(\Sigma^+ \rightarrow pX), \quad (\text{B8})$$

$$f_{\bar{n}}^{\bar{\Sigma}} = f_{\bar{p}}^{\text{Tan-Ng}} \kappa(\sqrt{s}) g_{\bar{\Sigma}^-}(x_R) \text{Br}(\Sigma^+ \rightarrow nX) + f_{\bar{p}}^{\text{Tan-Ng}} \kappa(\sqrt{s}) g_{\bar{\Sigma}^+}(x_R) \text{Br}(\Sigma^- \rightarrow nX). \quad (\text{B9})$$

The branching fractions for hyperon decays are $\text{Br}(\Lambda \rightarrow pX) \simeq 0.64$, $\text{Br}(\Lambda \rightarrow nX) \simeq 0.36$, $\text{Br}(\Sigma^+ \rightarrow pX) \simeq 0.52$, $\text{Br}(\Sigma^+ \rightarrow nX) \simeq 0.48$, and $\text{Br}(\Sigma^- \rightarrow nX) \simeq 1$ [59]. Summing up, we obtain Eq. (B5). We neglect the momentum difference between parent and daughter particles, since their mass difference is $\lesssim 20\%$.

2. Multiplicity of antihyperons at large \sqrt{s}

For relatively small $\sqrt{s} < 50$ GeV, we expect that Eq. (B5) holds with constant κ —namely, with weak \sqrt{s} dependence. This is because, empirically, radial scaling applies at small \sqrt{s} . However, when we consider large $\sqrt{s} > 50$ GeV, we have to consider the violation of radial scaling.

Reference [5] showed that the ratio between the multiplicity of antihyperons and \bar{p} is not constant as a function of \sqrt{s} . Following Ref. [5], we introduce \sqrt{s} dependence as an overall factor to the hyperon contributions, $\kappa(\sqrt{s})$, that satisfies $\lim_{s \rightarrow 0} \kappa(\sqrt{s}) = 1$ and deviates from unity at large \sqrt{s} .

We define the ratio between the multiplicity of $\bar{\Lambda}$ and \bar{p} at midrapidity:

$$\frac{\bar{\Lambda}}{\bar{p}} = \frac{dn_{\bar{\Lambda}}/dx_F}{dn_{\bar{p}}/dx_F} \Big|_{x_F=0}. \quad (\text{B10})$$

For simplicity, we assume that $\bar{\Lambda}, \bar{\Sigma}^{\pm}$ have the same scaling law for their multiplicity. By using this assumption, we take $\kappa(\sqrt{s})$ as

$$\kappa(\sqrt{s}) = \frac{(\bar{\Lambda}/\bar{p})(\sqrt{s})}{(\bar{\Lambda}/\bar{p})(0)}. \quad (\text{B11})$$

Finally, we analyze the ratio $\bar{\Lambda}/\bar{p}$ using data from STAR [60,61], ALICE [15,62], and CMS [18,63], which provides multiplicity ratios at midrapidity. NA49 also provides

⁴This conclusion is in some tension with the parallel discussion presented in Ref. [5], which will lead us to slightly different results.

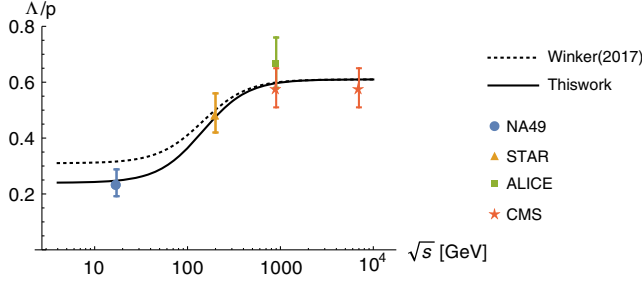


FIG. 8. $\bar{\Lambda}/\bar{p}$ ratio in proton-proton collision at midrapidity.

differential multiplicity at midrapidity; we assume an uncertainty of 20% from the uncertainty in the feed-down correction. This gives us $\bar{\Lambda}/\bar{p} = 0.24 \pm 0.05$ at $\sqrt{s} = 17.2$ GeV from the NA49 experiment.

Fig. 8 shows our result. For comparison, we also show $\bar{\Lambda}/\bar{p}$ as found in Ref. [5]. Our results can be fitted by the following formula:

$$\frac{\bar{\Lambda}}{\bar{p}} = 0.24 + \frac{0.37}{1 + ((146 \text{ GeV})^2/s)^{0.9}}. \quad (\text{B12})$$

3. Kinematical correction factors for antihyperon production

Let us determine $g_{\bar{B}}(x_R)$. NA49 analysis (see Fig. 22 in Ref. [21]) offers the differential multiplicity dn/dx_F for Λ , $\bar{\Lambda}$, Σ^+ , Σ^- , defined as

$$\frac{dn_{\bullet}}{dx_F}(x_F) = \frac{\pi}{\sigma^{\text{inel}}} \frac{\sqrt{s}}{2} \int dp_t^2 \frac{f_{\bullet}}{E}. \quad (\text{B13})$$

Uncertainties of dn/dx_F are not presented, but a typical error estimate of $\sim 20\%$ can be inferred from the analysis in Ref. [5].

Although the definition of $x_R (= E^*/E_{\text{max}}^*)$ and $x_F (= 2p_L^*/\sqrt{s})$ are different, their difference is of the order of p_t^2/s or m_p^2/s . Thus, $g_{\bar{B}}(x_R)$ can be determined from the observation of dn/dx_F . As discussed in Sec. II, $0.1 \lesssim x_R \lesssim 0.4$ is the important kinematical region to determine secondary cosmic ray production. In this region, the p_t dependence on E becomes weak and dn/dx_F is determined by the p_t weighted averaged cross section. In this respect, we find that dn/dx_F is a directly relevant quantity for secondary cosmic ray production. Then, it is reasonable to estimate

$$g_{\bar{B}}(x_R) = \left[\left(\frac{dn_{\bar{B}}}{dx_F} \right) / \left(\frac{dn_{\bar{p}}}{dx_F} \Big|_{\text{Tan-Ng}} \right) \right] \Big|_{x_F=x_R}, \quad (\text{B14})$$

with $\bar{B} = \Lambda, \bar{\Lambda}, \Sigma^+, \Sigma^-,$ or \bar{p} .

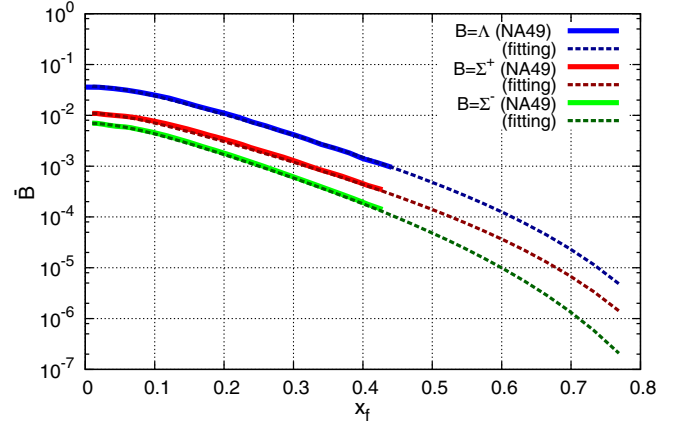


FIG. 9. x_F -dependent $\bar{B} \equiv dn_{\bar{B}}/dx_F$. The solid and dashed lines correspond to NA49 values and our fitting function, respectively.

Following Ref. [23], we assume the relation

$$\frac{dn_{\bar{\Sigma}^-}}{dx_F} \simeq 0.8 \times \frac{dn_{\bar{\Lambda}}/dx_F}{dn_{\Lambda}/dx_F} \frac{dn_{\Sigma^+}}{dx_F}. \quad (\text{B15})$$

Then, we expect

$$g_{\bar{\Sigma}^-} \simeq 0.8 \times \frac{dn_{\bar{\Lambda}}/dx_F}{dn_{\Lambda}/dx_F} g_{\Sigma^+}. \quad (\text{B16})$$

We assume a similar relation for $\bar{\Sigma}^+$:

$$g_{\bar{\Sigma}^+} \simeq 0.8 \times \frac{dn_{\bar{\Lambda}}/dx_F}{dn_{\Lambda}/dx_F} g_{\Sigma^-}. \quad (\text{B17})$$

To obtain $g_{\bar{B}}$, we fit the x_F dependence shown in the NA49 analysis by the following form:

$$g_{\bar{B}} = a(1 - x_R)^n. \quad (\text{B18})$$

We find $(a, n) = (0.13, -3)$, $(0.038, -3)$, and $(0.028, -2)$ well fit $\bar{\Lambda}$, $\bar{\Sigma}^-$, and $\bar{\Sigma}^+$, respectively.

Figure 9 shows the x_F -dependent $\bar{B} \equiv dn_{\bar{B}}/dx_F$. Solid and dashed lines correspond to NA49 values and our fitting function, respectively.

APPENDIX C: SECONDARY \bar{p}

Figure 10 shows the secondary \bar{p} cosmic ray flux predicted by our cross-section formula, calculated under the assumption that the mean target column density traversed by CR protons; He; nuclei such as B, C, and O; and \bar{p} is the same as the function of magnetic rigidity [32]. The column density used in the calculation is extracted from B/C data using fragmentation cross sections as specified in Ref. [24]. We consider the interactions

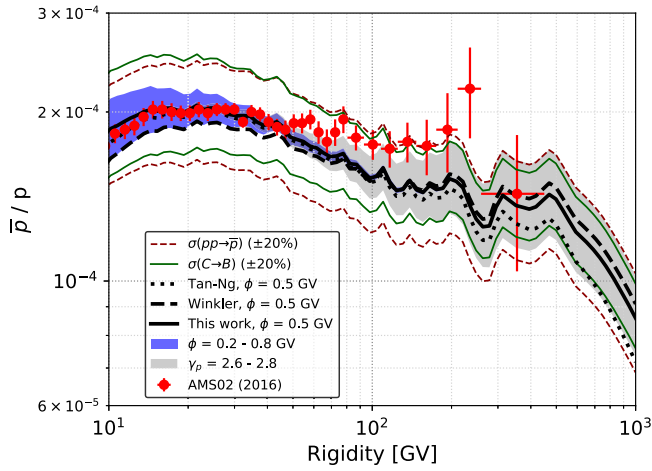


FIG. 10. Cosmic ray \bar{p} flux for several cross-section formulas. In all cases, we use the mean traversed target column density extracted from B/C data [32] using nuclear fragmentation cross sections as specified in Ref. [24]. The solid black line shows the prediction using our fit. All input nuclei, proton, and He spectra are taken from data. Dotted and dashed black lines show the results when using the fits from Tan and Ng [11] and Winkler [5], respectively. Other bands and lines show various sources of systematic uncertainty; see the text for details.

between ISM and cosmic rays for C, O, N, Ne, Mg, and Si. All nuclei, proton, and He spectra used in the calculation are taken directly from data (see Ref. [24] for more details).

The simple estimate in Fig. 10 is consistent with the AMS-02 \bar{p} data [3]. Above $\mathcal{R} \sim 100$ GV, the data rise above the central value of the prediction by $\sim 20\%$; however, systematic uncertainties due to the astrophysics and due to nuclear fragmentation cross sections, entering the calculation via the B/C analysis, prevent a clear conclusion. The calculation is sensitive to a number of systematic uncertainties. The blue region shows the uncertainty of the solar modulation parameter, $\phi = (0.2-0.8)$ GV. The gray region shows the result of varying the spectral index of proton CR above 300 GV. We vary γ_p in the range of 2.6–2.8, where $J_p \propto E_p^{-\gamma_p}$: this should represent the possibility that the CR proton spectrum in the regions dominating secondary \bar{p} production may not be identical to the locally measured spectrum. The solid green lines show the result of varying the C \rightarrow B fragmentation cross section by $\pm 20\%$. Finally, the dashed dark lines represent the \bar{p} -production cross section uncertainty of $\pm 20\%$.

- [1] L. Accardo *et al.* (AMS Collaboration), High Statistics Measurement of the Positron Fraction in Primary Cosmic Rays of 0.5–500 GeV with the Alpha Magnetic Spectrometer on the International Space Station, *Phys. Rev. Lett.* **113**, 121101 (2014).
- [2] M. Aguilar *et al.* (AMS Collaboration), Electron and Positron Fluxes in Primary Cosmic Rays Measured with the Alpha Magnetic Spectrometer on the International Space Station, *Phys. Rev. Lett.* **113**, 121102 (2014).
- [3] M. Aguilar *et al.* (AMS Collaboration), Antiproton Flux, Antiproton-to-Proton Flux Ratio, and Properties of Elementary Particle Fluxes in Primary Cosmic Rays Measured with the Alpha Magnetic Spectrometer on the International Space Station, *Phys. Rev. Lett.* **117**, 091103 (2016).
- [4] M. di Mauro, F. Donato, A. Goudelis, and P. D. Serpico, New evaluation of the antiproton production cross section for cosmic ray studies, *Phys. Rev. D* **90**, 085017 (2014).
- [5] M. W. Winkler, Cosmic ray antiprotons at high energies, *J. Cosmol. Astropart. Phys.* **02** (2017) 048.
- [6] F. Donato, M. Korsmeier, and M. Di Mauro, Prescriptions on antiproton cross section data for precise theoretical antiproton flux predictions, *Phys. Rev. D* **96**, 043007 (2017).
- [7] I. V. Moskalenko and A. W. Strong, Production and propagation of cosmic ray positrons and electrons, *Astrophys. J.* **493**, 694 (1998).
- [8] T. Delahaye, F. Donato, N. Fornengo, J. Lavalle, R. Lineros, P. Salati, and R. Taillet, Galactic secondary positron flux at the Earth, *Astron. Astrophys.* **501**, 821 (2009).
- [9] R. Kappl and A. Reinert, Secondary cosmic positrons in an inhomogeneous diffusion model, *Phys. Dark Universe* **16**, 71 (2017).
- [10] T. Kamae, N. Karlsson, T. Mizuno, T. Abe, and T. Koi, Parameterization of gamma, $e^{+/-}$ and neutrino spectra produced by p - p interaction in astronomical environment, *Astrophys. J.* **647**, 692 (2006); Erratum, *Astrophys. J.* **662**, 779(E) (2007).
- [11] L. C. Tan and L. K. Ng, Parametrization of hadron inclusive cross-sections in pp collisions extended to very low-energies, *J. Phys. G* **9**, 1289 (1983).
- [12] R. P. Feynman, Very High-Energy Collisions of Hadrons, *Phys. Rev. Lett.* **23**, 1415 (1969).
- [13] K. Kinoshita and H. Noda, Inclusive reactions and urbaryon rearrangement diagrams, *Prog. Theor. Phys.* **46**, 1639 (1971).
- [14] K. Kinoshita and H. Noda, Increase of single-particle spectra and a new form of scaling: Inclusive reactions and urbaryon rearrangement diagrams V, *Prog. Theor. Phys.* **49**, 896 (1973).
- [15] K. Aamodt *et al.* (ALICE Collaboration), Production of pions, kaons and protons in pp collisions at $\sqrt{s} = 900$ GeV with ALICE at the LHC, *Eur. Phys. J. C* **71**, 1655 (2011).

- [16] B. B. Abelev *et al.* (ALICE Collaboration), Production of charged pions, kaons and protons at large transverse momenta in pp and Pb-Pb collisions at $\sqrt{s_{NN}} = 2.76$ TeV, *Phys. Lett. B* **736**, 196 (2014).
- [17] J. Adam *et al.* (ALICE Collaboration), Measurement of pion, kaon and proton production in proton-proton collisions at $\sqrt{s} = 7$ TeV, *Eur. Phys. J. C* **75**, 226 (2015).
- [18] S. Chatrchyan *et al.* (CMS Collaboration), Study of the inclusive production of charged pions, kaons, and protons in pp collisions at $\sqrt{s} = 0.9, 2.76,$ and 7 TeV, *Eur. Phys. J. C* **72**, 2164 (2012).
- [19] A. Adare *et al.* (PHENIX Collaboration), Identified charged hadron production in $p + p$ collisions at $\sqrt{s} = 200$ and 62.4 GeV, *Phys. Rev. C* **83**, 064903 (2011).
- [20] I. Arsene *et al.* (BRAHMS Collaboration), Production of Mesons and Baryons at High Rapidity and High $P(T)$ in Proton-Proton Collisions at $\sqrt{s} = 200$ GeV, *Phys. Rev. Lett.* **98**, 252001 (2007).
- [21] C. Alt *et al.* (NA49 Collaboration), Inclusive production of charged pions in $p + p$ collisions at 158 GeV/ c beam momentum, *Eur. Phys. J. C* **45**, 343 (2006).
- [22] T. Anticic *et al.* (NA49 Collaboration), Inclusive production of charged kaons in $p + p$ collisions at 158 GeV/ c beam momentum and a new evaluation of the energy dependence of kaon production up to collider energies, *Eur. Phys. J. C* **68**, 1 (2010).
- [23] T. Anticic *et al.* (NA49 Collaboration), Inclusive production of protons, anti-protons and neutrons in $p + p$ collisions at 158 GeV/ c beam momentum, *Eur. Phys. J. C* **65**, 9 (2010).
- [24] K. Blum, K. C. Y. Ng, R. Sato, and M. Takimoto, Cosmic rays, anti-helium, and an old navy spotlight, *Phys. Rev. D* **96**, 103021 (2017).
- [25] M. Aguilar-Benitez *et al.*, Inclusive particle production in 400 GeV/ c pp interactions, *Z. Phys. C* **50**, 405 (1991).
- [26] B. Alper *et al.* (British-Scandinavian Collaboration), Production spectra of π^\pm, K^\pm, ρ^\pm at large angles in proton-proton collisions in the CERN Intersecting Storage Rings, *Nucl. Phys.* **B100**, 237 (1975).
- [27] P. Capiluppi, G. Giacomelli, A. M. Rossi, G. Vannini, A. Bertin, A. Bussiere, and R. J. Ellis, Charged particle production in proton-proton inclusive reactions at very high-energies, *Nucl. Phys.* **B79**, 189 (1974).
- [28] M. G. Albrow *et al.*, The distribution in transverse momentum of 5 GeV/ c secondaries produced at 53 GeV in the centre of mass, *Phys. Lett.* **42B**, 279 (1972).
- [29] M. G. Albrow *et al.* (CHLM Collaboration), Negative particle production in the fragmentation region at the CERN ISR, *Nucl. Phys.* **B56**, 333 (1973).
- [30] A. E. Brenner *et al.*, Experimental study of single particle inclusive hadron scattering and associated multiplicities, *Phys. Rev. D* **26**, 1497 (1982).
- [31] J. R. Johnson, R. Kammerud, T. Ohsugi, D. J. Ritchie, R. Shafer, D. Theriot, J. K. Walker, and F. E. Taylor, Inclusive charged hadron production in 100 GeV to 400 GeV pp collisions, *Phys. Rev. D* **17**, 1292 (1978).
- [32] B. Katz, K. Blum, J. Morag, and E. Waxman, What can we really learn from positron flux anomalies?, *Mon. Not. R. Astron. Soc.* **405**, 1458 (2010).
- [33] K. Blum, B. Katz, and E. Waxman, AMS-02 Results Support the Secondary Origin of Cosmic Ray Positrons, *Phys. Rev. Lett.* **111**, 211101 (2013).
- [34] T. Sjostrand, S. Mrenna, and P. Z. Skands, PYTHIA 6.4 physics and manual, *J. High Energy Phys.* **05** (2006) 026.
- [35] Y. Shikaze *et al.*, Measurements of 0.2 to 20 GeV/ n cosmic-ray proton and helium spectra from 1997 through 2002 with the BESS spectrometer, *Astropart. Phys.* **28**, 154 (2007).
- [36] M. Aguilar (AMS Collaboration), Precision Measurement of the Proton Flux in Primary Cosmic Rays from Rigidity 1 GV to 1.8 TV with the Alpha Magnetic Spectrometer on the International Space Station, *Phys. Rev. Lett.* **114**, 171103 (2015).
- [37] Y. S. Yoon *et al.*, Proton and helium spectra from the CREAM-III flight, *Astrophys. J.* **839**, 5 (2017).
- [38] R. Cowsik and B. Burch, On the positron fraction and the spectrum of the electronic component in cosmic rays, [arXiv:0905.2136](https://arxiv.org/abs/0905.2136).
- [39] B. Burch and R. Cowsik, On the positron fraction and cosmic-ray propagation models, [arXiv:1009.1361](https://arxiv.org/abs/1009.1361).
- [40] R. Cowsik, B. Burch, and T. Madziwa-Nussinov, The origin of the spectral intensities of cosmic-ray positrons, *Astrophys. J.* **786**, 124 (2014).
- [41] P. Blasi, The Origin of the Positron Excess in Cosmic Rays, *Phys. Rev. Lett.* **103**, 051104 (2009).
- [42] P. Blasi and P. D. Serpico, High-Energy Antiprotons from Old Supernova Remnants, *Phys. Rev. Lett.* **103**, 081103 (2009).
- [43] P. Mertsch and S. Sarkar, Testing Astrophysical Models for the PAMELA Positron Excess with Cosmic Ray Nuclei, *Phys. Rev. Lett.* **103**, 081104 (2009).
- [44] M. Ahlers, P. Mertsch, and S. Sarkar, On cosmic ray acceleration in supernova remnants and the FERMI/PAMELA data, *Phys. Rev. D* **80**, 123017 (2009).
- [45] M. Kachelriess, S. Ostapchenko, and R. Tomas, Antimatter production in supernova remnants, *Astrophys. J.* **733**, 119 (2011).
- [46] I. Cholis, D. Hooper, and T. Linden, Possible evidence for the stochastic acceleration of secondary antiprotons by supernova remnants, *Phys. Rev. D* **95**, 123007 (2017).
- [47] N. J. Shaviv, E. Nakar, and T. Piran, Natural Explanation for the Anomalous Positron to Electron Ratio with Supernova Remnants as the Sole Cosmic Ray Source, *Phys. Rev. Lett.* **103**, 111302 (2009).
- [48] M. Kachelrieß, A. Neronov, and D. V. Semikoz, Signatures of a Two Million Year Old Supernova in the Spectra of Cosmic Ray Protons, Antiprotons and Positrons, *Phys. Rev. Lett.* **115**, 181103 (2015).
- [49] B. C. Thomas, E. E. Engler, M. Kachelrieß, A. L. Melott, A. C. Overholt, and D. V. Semikoz, Terrestrial effects of nearby supernovae in the early Pleistocene, *Astrophys. J.* **826**, L3 (2016).
- [50] Y. Fujita, K. Kohri, R. Yamazaki, and K. Ioka, Is the PAMELA anomaly caused by the supernova explosions near the Earth?, *Phys. Rev. D* **80**, 063003 (2009).
- [51] K. Kohri, K. Ioka, Y. Fujita, and R. Yamazaki, Can we explain AMS-02 antiproton and positron excesses simultaneously by nearby supernovae without pulsars or dark matter?, *Prog. Theor. Exp. Phys.* **2016**, 021E01 (2016).

- [52] A. W. Strong, I. V. Moskalenko, and V. S. Ptuskin, Cosmic-ray propagation and interactions in the Galaxy, *Annu. Rev. Nucl. Part. Sci.* **57**, 285 (2007).
- [53] W. R. Webber and A. Soutoul, A study of the surviving fraction of the cosmic-ray radioactive decay isotopes ^{10}Be , ^{26}Al , ^{36}Cl and ^{54}Mn as a function of energy using the charge ratios Be/B, Al/Mg, Cl/Ar, and Mn/Fe measured on HEAO 3, *Astrophys. J.* **506**, 335 (1998).
- [54] K. Blum, Cosmic ray propagation time scales: Lessons from radioactive nuclei and positron data, *J. Cosmol. Astropart. Phys.* **11** (2011) 037.
- [55] P. Lipari, Interpretation of the cosmic ray positron and antiproton fluxes, *Phys. Rev. D* **95**, 063009 (2017).
- [56] C. Patrignani *et al.* (Particle Data Group), Review of particle physics, *Chin. Phys. C* **40**, 100001 (2016).
- [57] J. H. Scanlon and S. Milford, Energy spectra of electrons from π - μ - e decays in interstellar space, *Astrophys. J.* **141**, 718 (1965).
- [58] C. D. Dermer, Binary collision rates of relativistic thermal plasmas: II. Spectra, *Astrophys. J.* **307**, 47 (1986).
- [59] C. Patrignani *et al.* (Particle Data Group), Review of particle physics, *Chin. Phys. C* **40**, 100001 (2016).
- [60] B. I. Abelev *et al.* (STAR Collaboration), Strange particle production in $p + p$ collisions at $\sqrt{s} = 200$ GeV, *Phys. Rev. C* **75**, 064901 (2007).
- [61] B. I. Abelev *et al.* (STAR Collaboration), Systematic measurements of identified particle spectra in pp , d^+ Au and Au + Au collisions from STAR, *Phys. Rev. C* **79**, 034909 (2009).
- [62] K. Aamodt *et al.* (ALICE Collaboration), Strange particle production in proton-proton collisions at $\sqrt{s} = 0.9$ TeV with ALICE at the LHC, *Eur. Phys. J. C* **71**, 1594 (2011).
- [63] V. Khachatryan *et al.* (CMS Collaboration), Strange particle production in pp collisions at $\sqrt{s} = 0.9$ and 7 TeV, *J. High Energy Phys.* **05** (2011) 064.